analytical chemistry

pubs.acs.org/ac Article

Integrated 3D-Printed Hollow Microneedle Array and Lateral Flow Immunoassay for Point-of-Care Wound Healing Monitoring

Amadeo Sena-Torralba,*,○ Marc Parrilla,○ Ana Hernanz-Grimalt, Annemarijn Steijlen, Elena Ortiz-Zapater, Cristina Cabaleiro-Otero, Natividad López-Riquelme, Salvador Cerveró-Ferragut, Ángel Maquieira, Karolien De Wael, and Sergi Morais*

Cite This: *Anal. Chem.* 2024, 96, 20684−20692 Read Online

ACCESS | Metrics & More | Article Recommendations | Supporting Information

ABSTRACT: Chronic wound management requires continuous monitoring to assess healing and guide treatment. We developed a hollow microneedle array patch integrated with a lateral flow immunoassay strip to address the need for convenient, home-based diagnostics. This device extracts wound exudate directly from the wound matrix, overcoming the limitations of conventional swab sampling, which relies on surface exudate collection. The patch provides a minimally invasive, rapid solution to assess the wound healing phase. The immunoassay delivers a colorimetric signal visible to the naked eye, facilitating straightforward interpretation by clinicians within 10 min. In a clinical study involving 90 patients, matrix metalloproteinase 8 (MMP-8) was identified as a critical biomarker, achieving 80.3% sensitivity in detecting the proliferative phase. A specific lateral flow immunoassay for MMP-8 was developed with a detection limit of 0.7 ng/mL, lower than the threshold level for the proliferative healing phase (164.7 ng/mL). The hollow microneedle array patch was 3D-printed for cost-efficiency (less than €0.10 per patch) with a height of 865 ± 6 μm, allowing for a painless, easy sampling. Mechanical tests confirmed the durability of the patch, while cytotoxicity assays demonstrated its biocompatibility. Prevalidation using an *ex vivo* skin model showed the patch could extract 61 ± 6 μL of exudate, with a 122% recovery rate for MMP-8 detection, highlighting its efficiency in biomarker extraction. This approach represents a significant advance in decentralized wound care, offering a low-cost, user-friendly tool for at-home monitoring of chronic wounds, potentially improving early intervention and reducing hospital visits.

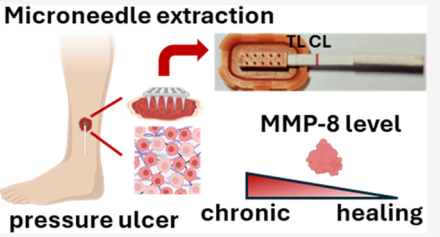

INTRODUCTION

Wound healing progresses through four phases: hemostasis (minutes to hours), inflammation (days 1−3), proliferation and repair (days 4−21), and remodeling (days 21−365).[1,2] Complex wounds often have prolonged inflammation, marked by increased MMP-8 activity, which indicates tissue damage and poor healing, making it a valuable biomarker.[3−5] Chronic wound treatment costs in Europe exceed €10.84 billion.[6] With rising rates of obesity, diabetes, and aging populations, the prevalence of chronic wounds is expected to grow, emphasizing the need for sensitive, reliable home tests for early diagnosis.

Current diagnostics mainly rely on pain assessment and visual inspection, while clinical guidelines recommend wound surface measurements, which are time-consuming and require expertise.[7,8] An alternative is using rapid diagnostic tests (RDTs) to analyze tissue, serum, or exudate biomarkers. Lateral flow immunoassays (LFIA) are promising for real-time monitoring due to their cost-effectiveness, ease of use, and rapid results.[9] Traditional sampling methods, like tissue biopsies and serum extraction, are invasive and labor-intensive.[10] Wound exudate, which reflects blood plasma and healing processes, offers a noninvasive alternative.[11] However, current methods for collecting wound exudate, such as swabbing, face challenges due to inconsistent exudate volume, accuracy, and the need for dilution, which complicates biomarker detection.[12−14]

We propose a novel hollow microneedle array (HMA) patch integrated with an LFIA strip to directly extract and analyze wound exudate, bypassing the need for surface sampling (Figure 1). While microneedles have been used in malaria and SARS-CoV-2 diagnostics, this is the first application in wound management validated with an ex vivo model.[15−18] The HMA pierces the wound for 10 min, allowing exudate to flow through the microneedles to the test strip, generating a quantifiable colorimetric signal via smartphone. Advantages include (i) consistent exudate collection, (ii) sufficient volume for LFIA without dilution, and (iii) rapid, on-site results for clinical decision-making. Despite concerns, the microneedles are minimally invasive, avoiding pain receptors and ensuring painless sampling, as shown in drug delivery studies.[19−21]

Received: October 22, 2024
Revised: December 3, 2024
Accepted: December 12, 2024
Published: December 17, 2024

https://doi.org/10.1021/acs.analchem.4c05688
Anal. Chem. 2024, 96, 20684−20692

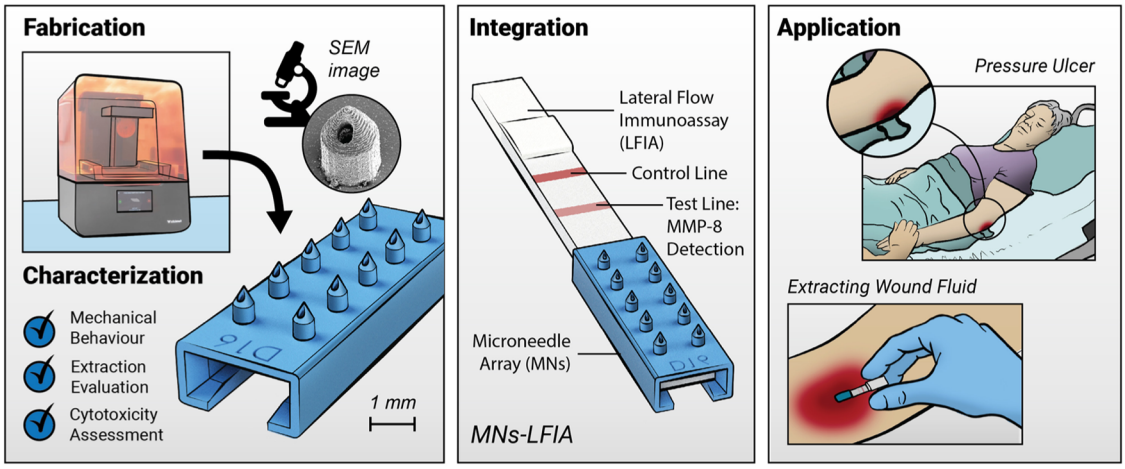

Figure 1. Schematic representation of the approach, showcasing the cost-effective 3D printing of a hollow microarray patch. When coupled with an LFIA strip, it enables single-step extraction of wound exudate fluid and detection of the MMP-8 healing biomarker.

We conducted a clinical study with exudate samples from 90 patients to assess MMP-8 as a wound-healing biomarker before developing the HMA-LFIA test. The HMA patch was fabricated using 3D stereolithography, achieving high resolution (tip sharpness <30 μm) and low cost (<€0.10 per patch) for scaling (Table S1).[22] After optimizing printing parameters, we tested the patch's piercing ability on Parafilm and porcine skin and evaluated its mechanical properties. We selected porcine skin since it is the most similar animal skin to human skin. Biocompatibility was confirmed with human epithelial cells. Using an ex vivo porcine wound model with agarose hydrogel, we ethically prevalidated the method, marking the first use of a hydrogel model for microneedle-based wound diagnostics. This advancement offers a critical step toward efficient exudate collection and biosensing, ensuring an accurate assessment of wound healing.

EXPERIMENTAL SECTION

The list of reagents, materials, instrumentation, and procedures, including the fabrication of the 3D-printed HMA, characterization of the HMA piercing, cytotoxicity tests, evaluation of the extraction capabilities of the integrated patch, detection of MMP-8 with HMA-LFIA, evaluation of HMA-LFIA in spiked samples, and *Ex vivo* assay for MMP-8 quantification using HMA-LFIA is provided in the Supplementary Data.

RESULTS AND DISCUSSION

Evaluation of MMP-8 as a Diagnostic Biomarker for Wound Healing. MMP-8 is the predominant collagenase found in both healing wounds and nonhealing ulcers,[23] and its concentration is a reliable biomarker for assessing wound status.[24] Elevated MMP-8 levels often indicate a chronic, nonhealing process.[25] Previous studies evaluating the diagnostic utility of MMP-8 have been limited by small and heterogeneous patient populations, leading to discrepancies and variability in the reported outcomes.[26] To better establish the relationship between MMP-8 levels and various wound healing phases, we analyzed 90 exudate samples from patients in the inflammatory, proliferative, and mixed (inflammatory and proliferative) phases using ELISA as the reference method. The calibration curve is shown in Figure S1. The analytical parameters of the ELISA calibration curve are provided in Table S2, and the results of the 90 exudate sample analyses are summarized in Table S3. The analysis identified 164.7 ng/mL as the threshold concentration, significantly differentiating the inflammatory phase from the proliferative and mixed phases (ANOVA, $p = 0.003$; Tukey, $p = 0.02$) (Table S4). Receiver operating characteristic (ROC) curve analysis demonstrated an area under the curve (AUC) of 0.80 ($p < 0.001$), indicating that the assay achieves 80.3% sensitivity in identifying pressure ulcers in the proliferative phase (Figure S2). These findings highlight the potential of the tested immunoreagents for developing valuable diagnostic devices to monitor wound healing, particularly in accurately differentiating inflammatory and proliferative phases.

Development of an LFIA for MMP-8 Quantification in Wound Exudate. Lateral flow immunoassays for detecting MMP-8 have been previously developed for diagnosing periodontitis,[27−29] but none have been reported for monitoring MMP-8 levels during wound healing. Earlier LFIA studies on wound healing have focused on detecting *P. aeruginosa* infection[30] or measuring C-reactive protein,[31] a nonspecific inflammatory marker that has proven to be an unreliable diagnostic biomarker for wound healing.[32] We developed a gold nanoparticle-based LFIA for MMP-8 quantification to address this gap. The calibration curve for MMP-8 (Figure 2A,B) revealed a LoD of 0.7 ng/mL and a LoQ of 1.1 ng/mL (Table S5).

This analytical performance surpasses many other colorimetric AuNP-based LFIAs developed for MMP-8 detection in different applications (Table S6).[33] This superior performance is attributed to using high-affinity commercial antibodies, which achieved a detection limit as low as 16 pg/mL in ELISA (Table S2).

The analytical parameters achieved are well-suited for monitoring MMP-8 levels during wound healing, as indicated by signal saturation at 100 ng/mL. This saturation threshold closely aligns with the MMP-8 concentration observed in the proliferative phase, which averages 164.7 ± 26.0 ng/mL (Table S4). Thus, a gradual signal decrease in the TL (Figure 2A) reports a transition to the proliferative phase and, hence, the successful healing of the wound.

Furthermore, precise quantification of MMP-8 levels in wound exudate samples can be achieved using the established calibration curve (Figure 2B). This capability underscores the

https://doi.org/10.1021/acs.analchem.4c05688
Anal. Chem. 2024, 96, 20684−20692

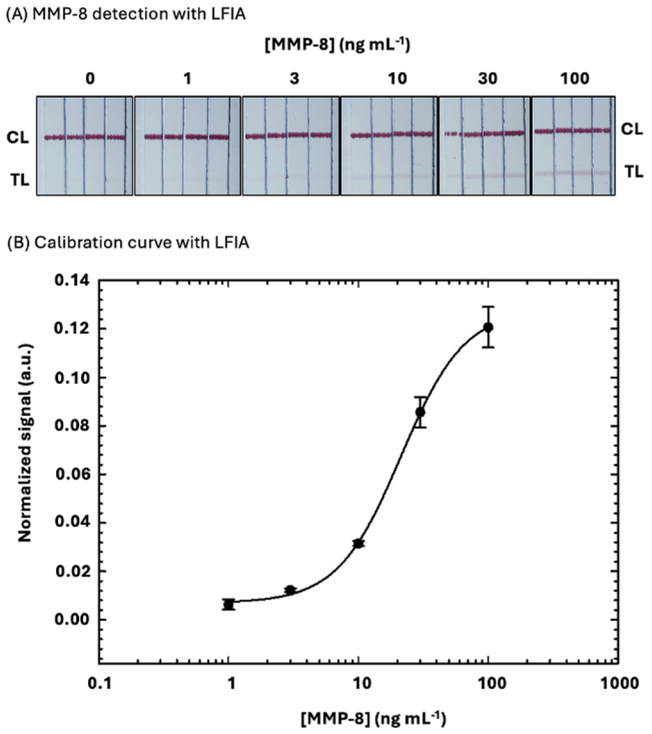

Figure 2. (A) Images of the LFIA strips after detecting MMP-8 in solution, using different concentrations of MMP-8 as shown in the images. (B) Calibration curve obtained with the LFIA in solution.

potential of the LFIA as a valuable diagnostic tool in assessing wound healing progress. By enabling real-time monitoring of MMP-8 concentrations, the LFIA can facilitate timely clinical interventions, allowing healthcare professionals to tailor treatments based on the healing phase. Additionally, the ability to distinguish between inflammatory and proliferative phases not only aids in diagnosing chronic wounds but also assists in evaluating the effectiveness of therapeutic strategies. As such, integrating this LFIA approach into clinical practice could significantly enhance patient outcomes by providing a rapid and accurate assessment of wound healing dynamics.

3D-Printed HMA Patch for Improved Exudate Sampling. Manufacturing an affordable HMA with precise features for painless piercing, such as small tip diameter, poses challenges due to the limitations of conventional 3D printing technology. Therefore, optimizing the parameters of stereolithography printing to achieve the sharpest microneedles while preventing clogging is essential. The HMA was designed with a bullet shape, featuring a base diameter of 0.6 mm, a height of 1.0 mm, a tip diameter of 20 μm, and a side hole with a diameter of 200 μm (Figure S3). This design facilitates both the optimization and evaluation of the 3D-printed HMA. A second model was created to ensure seamless integration with the LFIA while maintaining the exact microneedle dimensions (Figure S4). Figure S5A–D illustrates the top and bottom views of the HMA design integrated with the LFIA, while Figure S5E presents an optical microscope image of the microneedle. Figure 3A shows a scanning electron microscopy (SEM) image of the patch, with Figure 3B providing a close-up view of a single microneedle and an inset of its tip. Figure S6 offers a top view of the hollow microneedle. The SEM images reveal a distinct layer-by-layer printing structure. At the fastest printing speed, various exposure times (1, 1.5, and 2 s per layer) were assessed to optimize for the smallest tip diameter. Figure 3C indicates that an exposure time of 2 s yielded the most reliable tip size, with deviations from CAD of 11.0% for 2 s, 81.9% for 1.5 s, and 100.9% for 1 s. Figure S7 details the specific microneedle dimensions observed at different exposure times.

Furthermore, Figure 3D demonstrates the influence of layer height on dimensional deviations, establishing 20 μm as the optimal parameter for sharper tips, with deviations of 26.0% for 20 μm compared to 213.3% for 30 μm. Figure S8 provides the specific microneedle dimensions calculated at various layer heights. After optimization, the 3D-printed hollow microneedles exhibited a height of 865 $\pm$ 6 μm, a width of 439 $\pm$ 13 μm, a hole diameter of 142 $\pm$ 9 μm, and a tip diameter of 28 $\pm$ 1 μm (N = 3) (Figure 3E).

Ensuring the reliability of the printing process is critical for manufacturing reproducible patches, as variability in microneedle characteristics can significantly impact their effectiveness in clinical applications. Thus, intrabatch reproducibility was assessed by measuring five microneedles from three different batches. Figure 3F demonstrates excellent reproducibility for the optimized 3D-printing process, with dimensions of 856 $\pm$ 11 μm for height, 192.6 $\pm$ 8 μm for hole diameter, and 29 $\pm$ 2 μm for tip diameter (n = 15). These metrics confirm the reliability of the printing process and suggest that the HMA patch can consistently meet the design specifications necessary for practical wound exudate sampling. For additional details, Table S7 outlines the intramicroneedle reproducibility of each batch, Table S8 presents the intrapatch reproducibility, and Table S9 summarizes the intrabatch reproducibility. These findings collectively reinforce the reliability and consistency of the 3D-printed hollow microarray patches, highlighting their potential as a robust tool for wound exudate sampling and biomarker detection in clinical settings.

Mechanical Characterization of the 3D-Printed HMA Patch. To ensure that the 3D-printed patch can withstand the mechanical forces exerted during insertion into the skin or wound, we conducted a mechanical assessment using Parafilm as a skin simulant, a model widely recognized for evaluating microneedle robustness.[34,35]

A universal testing machine applied a constant force to the HMA patch while piercing the Parafilm. Previous studies have established that the forces typically used for piercing assessment range from 20 to 40 N, reflecting the average force exerted during thumb pressing.[34] After a 30-s insertion period, the HMA patch was removed, and the piercing depth through the Parafilm was determined by counting the number of holes in each layer, each layer representing a thickness of 127 μm (Figure 4A).

The bullet design of the HMA patch demonstrated optimal performance, achieving an insertion depth of 508 μm in 97.3% of the microneedles tested (n = 3). Figure S9 presents images of the Parafilm layers postassessment, while Figure S10 illustrates the displacement profiles of the HMA patch during the force application over 30 s. As observed in the manual Parafilm test results, greater force application increased insertion depth within the skin simulant. The results underscore the effectiveness of the HMA patch design in achieving the required piercing depth without compromising the integrity of the microneedles. This robust performance is crucial for applying the HMA in clinical settings, as it minimizes the risk of microneedle breakage or retention during use. Furthermore, the correlation between the applied force and the insertion depth emphasizes the importance of

https://doi.org/10.1021/acs.analchem.4c05688
Anal. Chem. 2024, 96, 20684−20692

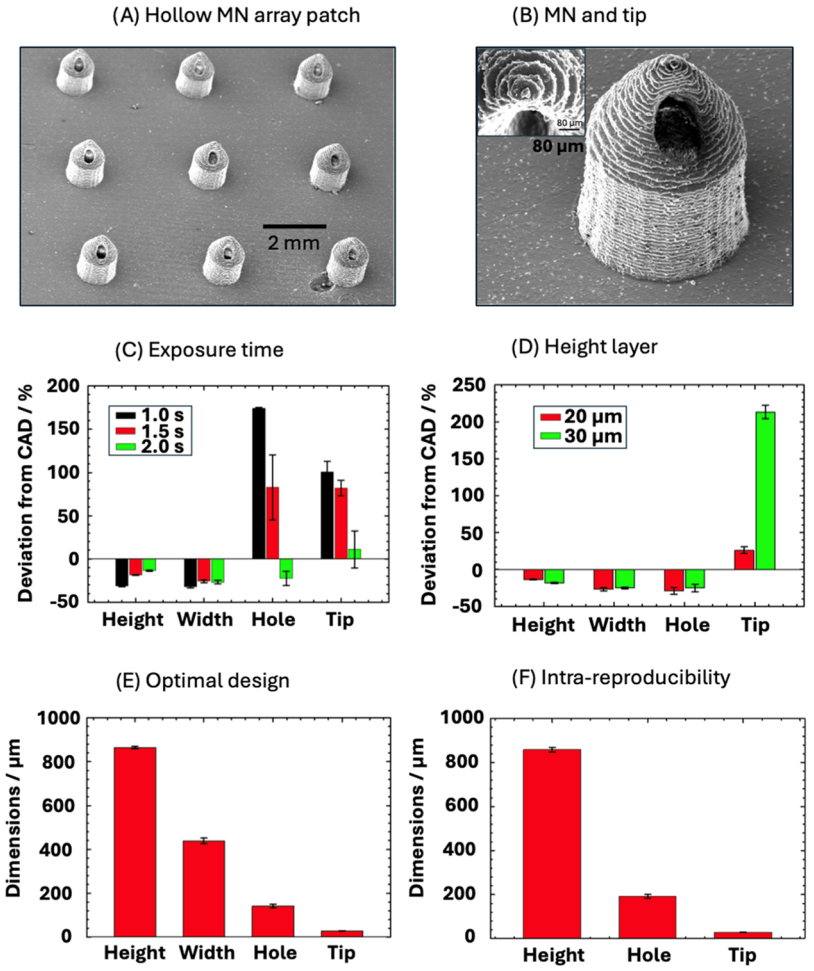

Figure 3. Design and evaluation of the 3D-printing capabilities: (A) SEM image of the HMA patch. (B) SEM image of a hollow microneedle, inset from the top view of a hollow microneedle, showing the hole and tip sharpness. Optimization of the (C) exposure time and (D) height layer on the printing capability of a 3D-printed HMA patch (N = 3). (E) HMA final dimensions after optimization (N = 3). (F) Intrabatch reproducibility of the 3D-printing method (N = 5).

precise force application during the patch, which can enhance the overall efficacy of wound exudate extraction.

Figure 4B illustrates the penetration depth measured by optical microscopy, corresponding to the transverse cuts shown in Figure 4C. The bullet HMA demonstrated notable piercing capabilities, with measured depths of 330 ± 21 μm at 20 N, 592 ± 16 μm at 30 N, and 721 ± 23 μm at 40 N. These results are particularly favorable when compared to previously reported 3D-printed HMA patches.[36−40] The exceptional performance of the bullet HMA can be attributed to the advanced printing capabilities of the 3D printer, which provides an xy resolution of 22 μm. In addition to assessing piercing capability, it is essential to evaluate the deformation of the microneedles following the mechanical tests. Height reduction and tip deformation of the microneedles (MNs) were quantified using ImageJ software before and after the mechanical testing (Figure 4D). The results, depicted in Figure 4E, show a slight height reduction of 2.5 ± 0.9% at 20 N, 2.3 ± 1.7% at 30 N, and 0.7 ± 0.2% at 40 N. Figure 4F presents the tip deformation measurements, showing deformations of 7.4 ± 2.1% at 20 N, 26.4 ± 6.9% at 30 N, and 16.7 ± 9.2% at 40 N. Notably, while the highest tip deformation occurred at 30 N, the MNs remained intact, demonstrating the robustness of the material during insertion.

The ability of the MNs to penetrate the skin was further assessed using optical coherence tomography, which employs a low-power infrared laser to image tissue up to 2 mm beneath the skin. The tomographic analysis was conducted after removing the HMA patch, as the polymeric nature of the HMA prevented imaging of the underlying tissue during patch application. Initially, the system was tested on Parafilm, with Figure S11 depicting images captured (A) before and (B) after piercing the Parafilm layers with the bullet HMA. Subsequently, porcine skin was analyzed following a 30 s thumb-pressing application of the HMA patch. Figure S12A shows the holes created by the MNs on the skin's surface, with the green arrows indicating the area imaged by the OCT. Figure S12B illustrates the disruption observed in the porcine skin when OCT imaging was performed at the center of the created holes. Despite the skin rapidly closing the holes post-removal of the HMA patch, the OCT images confirm the disruption, demonstrating the MNs' ability to reach the dermis layer. By proving that the MNs can penetrate the epidermis, the developed patch can access the soft tissue of a pressure injury characterized by an open wound lacking an epidermal layer. Given that the dermis is already accessible, the risk of infection during wound healing remains a significant concern. Therefore,

https://doi.org/10.1021/acs.analchem.4c05688
Anal. Chem. 2024, 96, 20684−20692

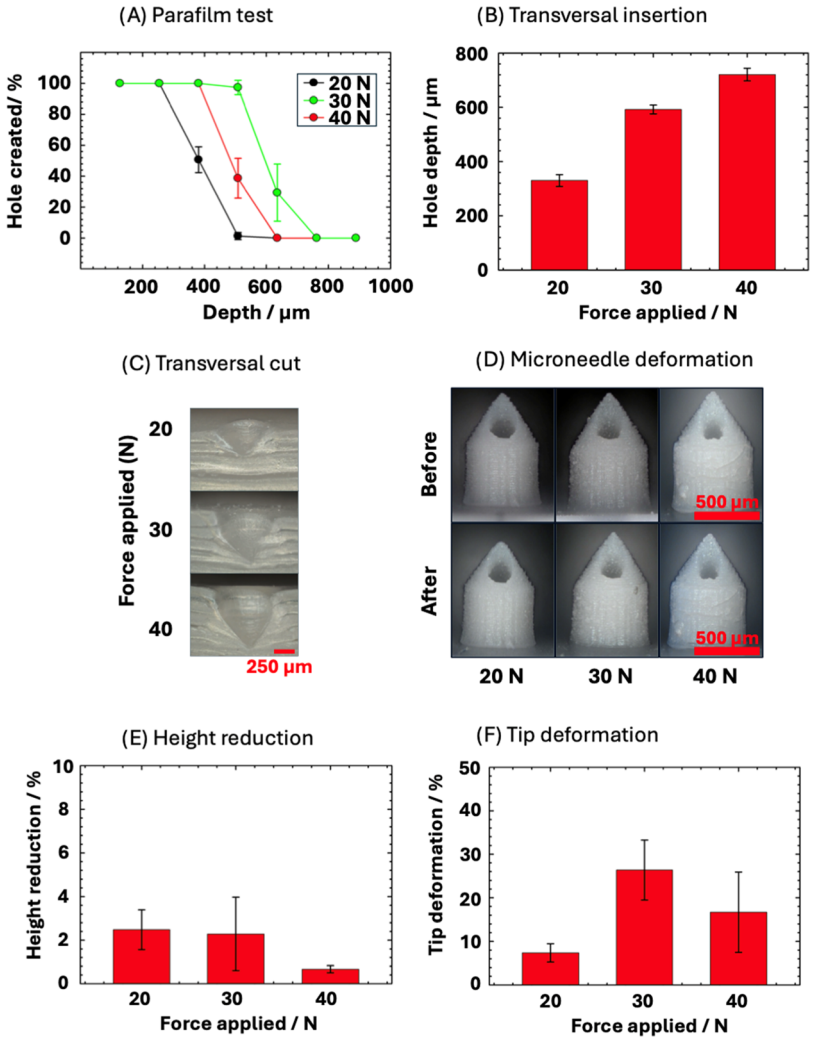

Figure 4. Evaluation of the mechanical strength and piercing capabilities using a universal testing machine on the Parafilm layers by applying forces of 20, 30, and 40 N. (A) Percentage of holes created by the HMA patches observed on each parafilm layer after the insertion test ($N = 3$). (B) Hole depth using the transversal cut test ($N = 3$). (C) Transversal cut of the Parafilm layers. (D) Optical microscope images of the hollow microneedle before and after performing the mechanical test. Evaluation of the percentage deformation after the mechanical test in Parafilm, (E) height reduction, and (F) tip deformation ($N = 3$).

it is imperative to utilize sterilized and biocompatible instrumentation to manage such conditions.

Cytotoxicity Assessment of the 3D-Printed HMA Patch. Ensuring the biocompatibility of the 3D-printed material is crucial for developing point-of-care testing devices. This assessment is critical because the MNs will come into contact with biofluids, and the 3D-printed resins may pose toxicity risks. A cytotoxicity assay was conducted by incubating hollow MNs with human epithelial cells for 2 days. Before incubation, the MNs were thoroughly rinsed and sterilized.

Building on our recent study, which identified Tween-20 as the most effective surfactant for enhancing the extraction capabilities of 3D-printed MNs,[31] we coated the HMA patch with Tween-20. The first column of Figure S13A presents images of three different cultured cell types, which were fixed and stained with DAPI before the MN immersion. Following this, the MNs and the Tween-20-coated MNs (MNs-T) were immersed in separate cell cultures for 10 min. A third culture, which did not receive MNs, served as a control. All cultures were incubated under identical conditions for 1 day (column 2) and 2 days (column 3). As shown, cells in all three cultures proliferated adequately, indicating that the MNs did not interfere with their proliferation rates.

Figure S13B illustrates the average cell counts in the three cultures at day 0 (before MN immersion), day 1, and day 2, demonstrating no significant decrease in cell proliferation in the presence of MNs. Additionally, preliminary incubation of the HMA with Tween-20 revealed no cytotoxic effects, indicating the safe potential use of Tween-20 to enhance the hydrophilicity of the MNs.

Evaluation of the Extraction Capabilities of the HMA-LFIA Test. The extraction process in the HMA-LFIA system is comprised of two integrated steps: (i) filling the HMA channels with wound exudate and (ii) subsequent absorption of the exudate onto the LFIA strip's sample pad via capillary action (Figure S5A). We employed a glass fiber membrane as the sample pad to optimize sample volume requirements, replacing the conventional cellulose membrane. This substitution was based on its nearly 2-fold reduction in thickness (0.43 mm vs 0.83 mm), thereby minimizing the volume needed for effective sample delivery to the other pads.

https://doi.org/10.1021/acs.analchem.4c05688
Anal. Chem. 2024, 96, 20684−20692

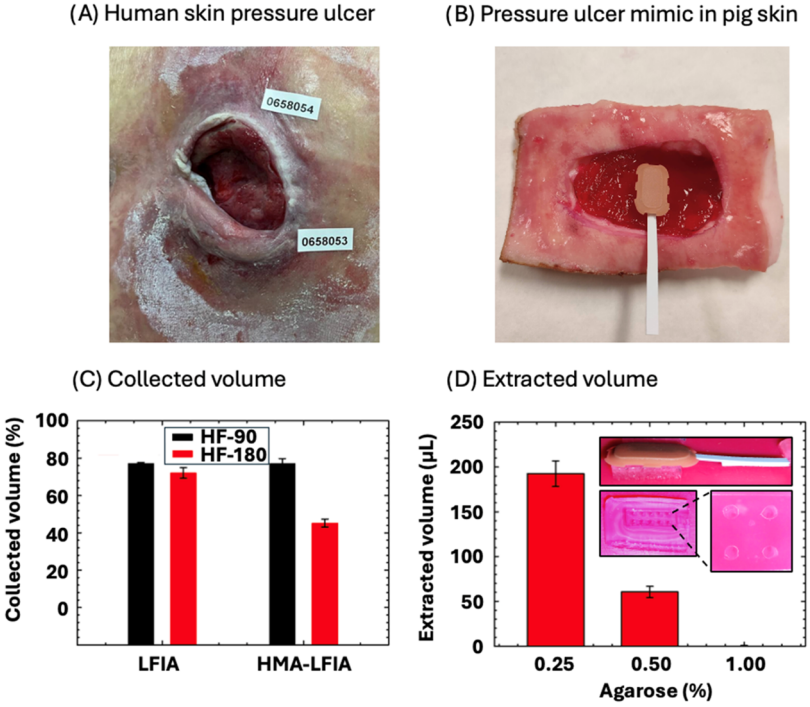

Figure 5. Evaluation of the extraction capability of the HMA-LFIA device using an ex vivo model. (A) Image of a pressure ulcer from which exudate samples were collected. (B) The ex vivo model was composed of porcine skin and agarose hydrogel. (C) Collected volume using LFIA strips and HMA-LFIA devices with nitrocellulose membranes HF-90 and HF-180, following the addition of 70 μL (N = 3). (D) Total extracted volume from agarose hydrogel (N = 3). Inset: HMA-LFIA piercing the hydrogel and magnified view of the hydrogel perforations.

Pressure ulcers, commonly resulting from prolonged pressure on the skin, are characterized by a loss of skin integrity, leading to open wounds where the dermis is exposed (Figure 5A). During the inflammatory phase of wound healing, exudate leaks from blood vessels.[5] Given the physiological properties of wound exudate from pressure ulcers, we developed a model mimicking the tissue environment. The model consisted of agarose gel (representing soft tissue) impregnated with phosphate-buffered saline (PBS) to simulate wound exudate, compressed between layers of porcine skin (representing hard tissue) (Figure 5B). Since a standardized agarose gel model for the extracellular matrix of open wounds does not yet exist, we tested the extraction performance of the HMA-LFIA using varying concentrations of agarose hydrogel (0.25, 0.5, and 1% agarose in PBS). To assess the extraction efficiency of the HMA, we applied a customized design for LFIA interfacing (Figure S5). LFIA strips were fabricated using detection pads with the highest and lowest flow rates, 90 s (HF-90) and 180 s (HF-180), for a 4 cm length of nitrocellulose membrane. The accuracy of our extraction measurement method was confirmed by the weight difference of LFIA strips (without attached HMA) after adding 70 μL of PBS to the sample pads. The average absorbed volume was 68 $\pm$ 1 μL (N = 3) and 70 $\pm$ 1 μL (N = 3) for LFIA strips with HF-90 and HF-180 pads, respectively. These results demonstrate that the evaluation method provided high accuracy (98.0%) and precision (98.8%).

When tested with the HMA-LFIA device, the collected volumes were 63 $\pm$ 2 μL (N = 3) and 45 $\pm$ 2 μL (N = 3) for HF-90 and HF-180, respectively, from a total volume of 70 μL (Figure 5C). HF-90 was selected for the HMA-LFIA system due to its superior collection efficiency, driven by its faster capillary flow rate. These findings confirmed the pivotal role of the LFIA strip in determining the extraction rate of the HMA. Faster flow rates in the LFIA strip directly correlated with higher exudate extraction rates, underscoring the importance of complete system integration.

The extraction efficiency in the hydrogel model was assessed using the same methodology. After a 10 min insertion of the HMA-LFIA device into the hydrogel, we collected 193 $\pm$ 14 μL (N = 3), 61 $\pm$ 6 μL (N = 3), and 0 μL (N = 3) from 0.25, 0.5, and 1% agarose gels, respectively (Figure 5D). Although direct comparisons between agarose gels and open wounds are complex, 0.5% agarose was deemed the most representative of wound exudate from pressure ulcers, as it balanced moisture content, being less liquid than 0.25% agarose but less dry than 1% agarose. As expected, the extracted volume decreased with increasing gel density, validating that the HMA-LFIA can extract fluid from a semisolid matrix akin to a wound in the inflammatory phase. Notably, the extracted volume was sufficient to conduct the LFIA assay. For reference, a conventional 3.0 mm-wide LFIA strip typically requires 70 μL of sample.[41] By reducing the strip width to 2.5 mm, we reduced the necessary sample volume to 40 μL, sufficient to rehydrate the conjugate pad and allow capillary flow to reach the absorbent pad.

Analysis of MMP-8 with the HMA-LFIA Test. The integrated HMA-LFIA test was first evaluated using serial dilutions of MMP-8 in PBS. The test demonstrated an average recovery of 130 $\pm$ 13% across MMP-8 concentrations close to the EC50 of the calibration curve at 3, 10, and 30 ng/mL (Table S10). These results confirm that the HMA can effectively collect and transfer MMP-8 to the LFIA strip without significant loss due to nonspecific adsorption to the HMA resin (Figure S14). Next, the performance of the HMA-LFIA was assessed using an *ex vivo* ulcer model with a 0.5%

https://doi.org/10.1021/acs.analchem.4c05688
Anal. Chem. 2024, 96, 20684−20692

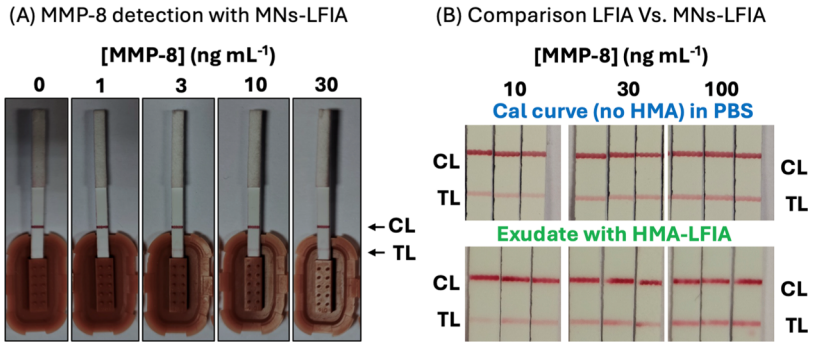

Figure 6. Analysis of MMP-8 in wound exudates using the HMA-LFIA system. (A) Image of HMA-LFIA strips showing detection of MMP-8 at various concentrations in the ex vivo ulcer model (B) Comparison of signal intensity obtained with LFIA and HMA-LFIA strips for quantifying MMP-8 in PBS and exudate, respectively.

agarose hydrogel. The extracted exudate volume from the hydrogel was sufficient to rehydrate the conjugate pad and deliver the sample to the TL and the CL. Notably, the CL consistently exhibited a strong and stable signal, indicating that the exudate composition did not interfere with the functionality of the LFIA or the interpretation of results (Figure 6A). The CL, a positive control, confirmed that sufficient sample volume was delivered. Moreover, the low coefficient of variation (3% RSD) across 12 replicates of the CL signal demonstrated the high reproducibility of the HMA in delivering the sample at an optimal flow rate, avoiding overloading of the detection pad.

The HMA-LFIA system showed consistent signal intensities at the TL, correlating with MMP-8 concentrations in hydrogel (Figure 6B). Average recovery was 122 ± 38% at 10, 30, and 100 ng/mL in exudate samples (Table S11), with nearly 100% recovery at concentrations close to the EC50 (21.29 ng/mL). Recovery decreased at concentrations above the LDR (57.36 ng/mL), e.g., 100 ng/mL showed 178% recovery. A paired *t*test confirmed the HMA-LFIA's accuracy (P = 0.38) for MMP-8 quantification (<164.7 ng/mL) within the LDR in 10 min compared to the ELISA method. The assay can be further optimized to extend the LDR for inflammatory and proliferative phase MMP-8 levels. High reproducibility highlights its potential for minimally invasive, precise fluid extraction and in situ analysis.

CONCLUSIONS

This study presents a 3D-printed hollow microarray patch integrated with a lateral flow immunoassay (HMA-LFIA) for monitoring MMP-8 levels in wound exudate. The HMA-LFIA offers a reliable, minimally invasive method for real-time wound healing assessment, particularly distinguishing between inflammatory and proliferative phases. It demonstrated high analytical performance, detecting MMP-8 at 0.7 ng/mL, with signal saturation at 100 ng/mL, corresponding to proliferative phase concentrations. Optimized for efficient exudate extraction, the patch showed precise dimensions, mechanical strength, and cytocompatibility. Using an ex vivo ulcer model, it successfully extracted and quantified wound exudate, validating its potential for clinical monitoring. This system advances point-of-care diagnostics by combining a 3D-printed collection device with a sensitive LFIA, enabling personalized, effective wound care and timely interventions.

ASSOCIATED CONTENT

Supporting Information

The Supporting Information is available free of charge at https://pubs.acs.org/doi/10.1021/acs.analchem.4c05688.

Additional experimental details of the materials, reagents, and instruments used, and methods for the fabrication and optimization of the 3D-printed HMA patch, evaluation of the piercing capability, modification of the HMA patch, cytotoxicity evaluation, evaluation of clinical samples with ELISA, evaluation of the extraction capability of the HMA patch and LFIA strip's fabrication. Tables showing raw data on the analytical parameters of the assays, levels of MMP-8 in exudate samples of patients, dimensions of the hollow microneedles, and assay recoveries when analyzing exudate samples with HMA-LFIA. Additional figures and photographs related to the characterization of the HMA patch and analytical characterization of the HMA-LFIA (PDF)

AUTHOR INFORMATION

Corresponding Authors

Amadeo Sena-Torralba − *Instituto Interuniversitario de Investigación de Reconocimiento Molecular y Desarrollo Tecnológico (IDM), Universitat Politècnica de València, Universitat de València, 46022 Valencia, Spain;* orcid.org/0000-0003-1340-1383; Email: asentor@upvnet.upv.es

Sergi Morais − *Instituto Interuniversitario de Investigación de Reconocimiento Molecular y Desarrollo Tecnológico (IDM), Universitat Politècnica de València, Universitat de València, 46022 Valencia, Spain; Departamento de Química, Universitat Politècnica de València, 46022 Valencia, Spain;* orcid.org/0000-0002-3722-2358; Email: smorais@upv.es

Authors

Marc Parrilla − *A-Sense Lab, University of Antwerp, 2010 Antwerp, Belgium; NANOlab Center of Excellence, University of Antwerp, 2010 Antwerp, Belgium;* orcid.org/0000-0002-1344-8432

Ana Hernanz-Grimalt − *Instituto Interuniversitario de Investigación de Reconocimiento Molecular y Desarrollo Tecnológico (IDM), Universitat Politècnica de València, Universitat de València, 46022 Valencia, Spain*

https://doi.org/10.1021/acs.analchem.4c05688
Anal. Chem. 2024, 96, 20684−20692

Annemarijn Steijlen − *A-Sense Lab, University of Antwerp, 2010 Antwerp, Belgium; NANOlab Center of Excellence, University of Antwerp, 2010 Antwerp, Belgium;* orcid.org/0000-0003-2838-7799
Elena Ortiz-Zapater − *Department of Biochemistry and Molecular Biology, Universitat de Valencia, 46010 Valencia, Spain; Instituto Investigación Hospital Clínico-INCLIVA, 46010 Valencia, Spain*
Cristina Cabaleiro-Otero − *Hospital General Universitario de Elche, 03203 Elche, Alicante, Spain*
Natividad López-Riquelme − *Hospital General Universitario de Elche, 03203 Elche, Alicante, Spain*
Salvador Cerveró-Ferragut − *Hospital General Universitario de Elche, 03203 Elche, Alicante, Spain*
Ángel Maquieira − *Instituto Interuniversitario de Investigación de Reconocimiento Molecular y Desarrollo Tecnológico (IDM), Universitat Politècnica de València, Universitat de València, 46022 Valencia, Spain; Departamento de Química, Universitat Politècnica de València, 46022 Valencia, Spain;* orcid.org/0000-0003-4641-4957
Karolien De Wael − *A-Sense Lab, University of Antwerp, 2010 Antwerp, Belgium; NANOlab Center of Excellence, University of Antwerp, 2010 Antwerp, Belgium;* orcid.org/0000-0003-4495-0748

Complete contact information is available at: https://pubs.acs.org/10.1021/acs.analchem.4c05688

Author Contributions

○A.S.-T. and M.P. contributed equally to this work. A.S.-T.: Investigation, Methodology, Data curation, Formal analysis, Validation, Visualization, Writing - original draft. M.P.: Conceptualization, Data curation, Formal analysis, Investigation, Methodology, Validation, Visualization, Writing - original draft. A.H.-G.: Investigation, Formal analysis. A.S.: Investigation, Methodology, Formal analysis, Visualization, Writing - review and editing. E.O.-Z.: Investigation, Methodology, Formal analysis, Writing - review and editing. C.C.-O.: Investigation, Methodology, Formal analysis. N.L.-R.: Investigation, Methodology, Formal analysis. S.C.-F.: Investigation, Methodology, Formal analysis. Á.M.: Writing - review and editing, Funding. K.D.W.: Writing - review and editing, Resources. S.M.: Writing - review and editing, Funding.

Notes

The authors declare no competing financial interest.

■ ACKNOWLEDGMENTS

A.S.-T. acknowledges Generalitat Valenciana and the European Social Fund for the CIAPOS fellowship (CIAPOS/2022/7) and the Incoming Mobility Stay fellowship of FWO in Flanders, Belgium (V510323N). M.P. acknowledges the support of the Fund for Scientific Research (FWO) in Flanders (K217022N and 1265223N), Belgium. A.H.-G. acknowledges the fellowship Programa Investigo 2022 funded by the European Union − NextGenerationEU. A.S. recognizes support through a Rubicon fellowship from the Dutch Research Council (019.223EN.003). The research was financed by the UPP-DIAGNOSTIC 202-AP-13 grant from UniSalut Polisabio. The authors acknowledge BOF-UAntwerp, FWO infrastructure funding.

■ REFERENCES

(1) Olsson, M.; Järbrink, K.; Divakar, U.; Bajpai, R.; Upton, Z.; Schmidtchen, A.; Car, J. *Wound Repair Regen.* **2019**, *27*, 114−125.
(2) Wilkinson, H. N.; Hardman, M. J. *Open Biol.* **2020**, *10*, No. 200223.
(3) Lu, S. H.; Samandari, M.; Li, C.; Li, H.; Song, D.; Zhang, Y.; Tamayol, A.; Wang, X. *Sens. Actuators Rep.* **2022**, *4*, No. 100075.
(4) Stacey, M. C.; Phillips, S. A.; Farrokhyar, F.; Swaine, J. M. *Wound Repair Regen.* **2019**, *27*, 509−518.
(5) Goto, T.; Saligan, L. N. *J. Wound Ostomy Cont. Nurs.* **2020**, *47*, 559−568.
(6) Queen, D.; Harding, K. *Int. Wound J.* **2024**, *21*, No. e14709.
(7) Powers, J. G.; Higham, C.; Broussard, K.; Phillips, T. J. *J. Am. Acad. Dermatol.* **2016**, *74*, 607−625.
(8) Wendland, D. M.; Tailor, D. W. M. *J. Acute Care Phys. Therapy* **2017**, *8*, 42−57.
(9) Parolo, C.; Sena-Torralba, A.; Bergua, J. F.; Calucho, E.; Fuentes-Chust, C.; Hu, L.; Rivas, L.; Álvarez-Diduk, R.; Nguyen, E. P.; Cinti, S.; Quesada-González, D.; Merkoçi, A. *Nat. Protoc.* **2020**, *15*, 3788−3816.
(10) Mota, F. A. R.; Pereira, S. A. P.; Araújo, A. R. T. S.; Passos, M. L. C.; Saraiva, M.L.M.F.S. *Trends Anal. Chem.* **2021**, *143*, No. 116405.
(11) McIntosh, C.; Ivory, J. D.; Gethin, G. *Diabet Foot J.* **2019**, *22*, 46−53.
(12) Cross, H. H. *Nursing* **2014**, *44*, 68−69.
(13) Fletcher, J. *Nurs. Times.* **2003**, *99* (5), 51−52.
(14) White, R.; Cutting, K. F. Wound exudate: effective assessment and management *World Wide Wounds*, **2006** *1*.
(15) Chen, Y. J.; Hsu, Y. P.; Tain, Y. L.; Li, N. S.; Pang, H. H.; Kuo, S. W.; Yang, H. W. *Biosens. Bioelectron.* **2022**, *208*, No. 114234.
(16) Jiang, X.; Lillehoj, P. B. *Microsyst. Nanoeng.* **2020**, *6*, 1−11.
(17) Bao, L.; Park, J.; Qin, B.; Kim, B. *Sci. Rep.* **2022**, *12*, No. 10693.
(18) Turner, J. G.; Lay, E.; Jungwirth, U.; Varenko, U.; Gill, H. S.; Estrela, P.; Leese, H. S. *Adv. Mater. Technol.* **2023**, *8*, No. 2300259.
(19) Ghiyasi, Y.; Prewett, P. D.; Davies, G. H.; Rad, Z. F. *Int. J. Pharm.* **2023**, *641*, No. 123087.
(20) Barnum, L.; Samandari, M.; Schmidt, T. A.; Tamayol, A. *Expert Opinion Drug Delivery* **2020**, *17*, 1767−1780.
(21) Haidari, H.; Bright, R.; Yu, Y.; Vasilev, K.; Kopecki, Z. *Small Sci.* **2024**, *4*, No. 2400158.
(22) Shahrubudin, N.; Lee, T. C.; Ramlan, R. *Procedia Manufact.* **2019**, *35*, 1286−1296.
(23) Nwomeh, B. C.; Liang, H. X.; Cohen, I. K.; Yager, D. R. *J. Surg. Res.* **1999**, *81*, 189−195.
(24) Amato, B.; Coretti, G.; Compagna, R.; Amato, M.; Buffone, G.; Gigliotti, D.; Grande, R.; Serra, R.; de Franciscis, S. *Int. Wound J.* **2015**, *12*, 641−645.
(25) Dissemond, J.; Augustin, M.; Dietlein, M.; Faust, U.; Keuthage, W.; Lobmann, R.; Münter, K. C.; Strohal, R.; Stücker, M.; Traber, J.; Vanscheidt, W.; Läuchli, S. *J. Wound Care* **2020**, *29*, 102−118.
(26) Lazaro, J. L.; Izzo, V.; Meaume, S.; Davies, A. H.; Lobmann, R.; Uccioli, L. *J. Wound Care* **2016**, *25*, 277−287.
(27) Yee, E. H.; Lathwal, S.; Shah, P. P.; Sikes, H. D. *ACS Sens.* **2017**, *2*, 1589−1593.
(28) Johnson, N.; Ebersole, J.; Kryscio, R.; Danaher, R.; Dawson, D.; Al-Sabbagh, M.; Miller, C. *Oral Dis.* **2016**, *22*, 681−687.
(29) He, W.; You, M.; Li, Z.; Cao, L.; Xu, F.; Li, F.; Li, A. *Sensors Actuators, B Chem.* **2021**, *334*, No. 129673.
(30) Klebes, A.; Kittel, A. S.; Verboket, R. D.; von Stetten, F.; Früh, S. M. *Sensors Actuators B Chem.* **2022**, *355*, No. 131283.
(31) Downs, C.; Milovancev, M.; Fu, E. *Talanta* **2020**, *220*, No. 121319.
(32) Kindsley, A.; Jones, V. *Wounds UK* **2008**, *4*, 32−46.
(33) Sena-Torralba, A.; Álvarez-Diduk, R.; Parolo, C.; Piper, A.; Merkoçi, A. *Chem. Rev.* **2022**, *122*, 14881−14910.
(34) Larrañeta, E.; Moore, J.; Vicente-Pérez, E. M.; González-Vázquez, P.; Lutton, R.; Woolfson, A. D.; Donnelly, R. F. *Int. J. Pharm.* **2014**, *472*, 65−73.

(35) Anjani, Q. K.; Nainggolan, A. D. C.; Li, H.; Miatmoko, A.; Larrañeta, E.; Donnelly, R. F. *Int. J. Pharm.* **2024**, *655*, No. 124071.
(36) Mathew, E.; Pitzanti, G.; Gomes dos Santos, A. L.; Lamprou, D. A. *Pharmaceutics* **2021**, *13*, 1837.
(37) Economidou, S. N.; Uddin, M. J.; Marques, M. J.; Douroumis, D.; Sow, W. T.; Li, H.; Reid, A.; Windmill, J. F. C.; Podoleanu, A. *Addit. Manuf.* **2021**, *38*, No. 101815.
(38) Xenikakis, I.; Tzimtzimis, M.; Tsongas, K.; Andreadis, D.; Demiri, E.; Tzetzis, D.; Fatouros, D. G. *Eur. J. Pharm. Sci.* **2019**, *137*, No. 104976.
(39) Uddin, M. J.; Scoutaris, N.; Economidou, S. N.; Giraud, C.; Chowdhry, B. Z.; Donnelly, R. F.; Douroumis, D. *Mater. Sci. Eng. C* **2020**, *107*, No. 110248.
(40) Parrilla, M.; Sena-Torralba, A.; Steijlen, A.; Morais, S.; Maquieira, Á.; De Wael, K. *Biosens. Bioelectron.* **2024**, *251*, No. 116131.
(41) Sena-Torralba, A. S.; Ngo, D. B.; Parolo, C.; Hu, L.; Álvarez-Diduk, R.; Bergua, J. F.; Rosati, G.; Surareungchai, W.; Merkoçi, A. *Biosen. Bioelectron.* **2020**, *168*, No. 112559.

https://doi.org/10.1021/acs.analchem.4c05688
Anal. Chem. 2024, 96, 20684−20692